PTEP

Prog. Theor. Exp. Phys. **2014**, 06B107 (27 pages)
DOI: 10.1093/ptep/ptu066

CMB Cosmology

CMB spectral distortions and energy release in the early universe

Hiroyuki Tashiro[1,2,*]

[1]*Physics Department, Arizona State University, Tempe, Arizona 85287, USA*
[2]*Department of Physics and Astrophysics, Nagoya University, Nagoya 464-8602, Japan*
[*]E-mail: hiroyuki.tashiro@nagoya-u.jp

Received February 24, 2014; Revised April 17, 2014; Accepted April 25, 2014; Published June 11, 2014

Measuring the spectral deviation of the cosmic microwave background (CMB) from the blackbody spectrum has become a focus of attention as a probe of the thermal history of the Universe. It has been more than 20 years since COBE/FIRAS's measurement, which showed excellent agreement between the CMB spectrum and a perfect blackbody spectrum. Significant developments in the technology since then have allowed us to improve the sensitivity of the absolute spectrum measurement by a factor of $\sim 10^4$. Therefore, the physics related to the generation of CMB spectral distortions should now be investigated in greater detail. To probe the physics in the early universe and to open an observational window for new physics, various energy release mechanisms both in and beyond standard cosmology need to be studied. In this paper, we provide a review of the physics of CMB distortions and the energy release that creates CMB distortions in the early universe.

Subject Index E63, E65

1. Introduction

The blackbody spectrum of the cosmic microwave background (CMB) is a key prediction of the Big Bang theory. After Penzias and Wilson's discovery of the CMB in 1965 [91], there were several early attempts to measure the frequency spectrum of the CMB. Observational results in the Rayleigh–Jeans part strongly supported the blackbody spectrum of the CMB [36], while the spectral shape in the Wien part was the subject of controversy because of the difficulties of the measurements. A remarkable achievement was established by the Far InfraRed Absolute Spectrophotometer (FIRAS) on-board the COsmic Background Explorer (COBE) satellite. It revealed that the CMB spectrum is extremely close to a perfect blackbody of a temperature $T_0 = 2.725 \pm 0.001\,\mathrm{K}$, and the possible deviation from the blackbody is limited to $\Delta I_\nu / I_\nu \lesssim 10^{-5}$ [31,74]. There was no detection of CMB distortions from the blackbody spectrum. After this precise measurement, the primary concern in the CMB spectrum shifted to how much, if at all, the CMB spectrum deviates from the blackbody spectrum.

The thermalization process of the CMB in the early universe has long been studied. In the early universe (redshift $z \gtrsim 2 \times 10^6$), a blackbody spectrum is maintained by a combination of processes such as Compton scattering, bremsstrahlung [51,52,113], and double Compton scattering [11,26]. However, due to the expansion of the Universe, these interactions become less efficient with time.

As a result, energy injected at epochs $z < 10^6$ can induce deviation from the blackbody spectrum. That is, CMB spectral distortions are created.

The type of CMB distortions generated depends on the epoch of the energy release. Commonly, CMB distortions are classified into two types of distortions: μ-type and y-type distortions [113,133]. The evolution of these distortions has been studied both analytically and numerically [10,11,20,25,26,47,60,110]. The μ-type distortion is characterized by a frequency-dependent chemical potential. This distortion is created between the double Compton scattering decoupling ($z \sim 10^6$) and the thermalization decoupling by Compton scattering ($z \sim 10^5$). On the other hand, the y-type distortion is produced after the thermalization decoupling by Compton scattering. Therefore, measurement of these CMB distortions is a powerful tool for investigating the thermal history of the Universe.

Recently, two future missions, PIXIE and PRISM, have been proposed for precise measurement of the CMB distortions. At present, the CMB distortions are tightly constrained by COBE/FIRAS; $|\mu| < 9 \times 10^{-5}$ and $y < 1.5 \times 10^{-5}$ [31]. The sensitivities of PIXIE and PRISM for measuring CMB distortions will be dramatically improved, making them able to detect the CMB distortions with $\mu \sim 10^{-8}$ or $y \sim 10^{-8}$. Therefore, CMB distortions are attracting a great deal of attention as an important new probe of physics in the early universe.

There are many kinds of generation mechanisms for CMB distortions in the early universe. In standard cosmology, CMB distortions are created by the Silk damping of small-scale perturbations [4,24,46,111] and the cooling of photons by electrons and baryons [62]. The mechanisms beyond the standard model include the decay and annihilation of relic particles [17,22,48,76], primordial magnetic fields [54,68,80], and so on. Therefore, detection of or constraints on CMB distortions can provide us with direct access to the early universe and high-energy physics. In this paper, we review various generation mechanisms that create CMB distortions in the early universe, including recent developments.

The paper is organized as follows. In Sect. 2, we describe the interactions between photons and electrons, which play crucial roles in the thermalization process of the CMB. In Sect. 3, we review the types of CMB distortions, deriving the analytic spectral forms in some limits. In Sect. 4, we summarize the current constraint on the CMB distortions and future missions for measuring the CMB frequency spectrum. In Sect. 5, we review various mechanisms for CMB distortions in the early universe. In Sect. 6, future prospects are provided. Throughout this paper, we use the natural units $c = \hbar = 1$ and we set the Boltzmann constant $k_{\rm B}$ to 1.

2. Boltzmann equation for the CMB thermalization process

CMB spectral distortions are signatures of energy release in the early universe. Suppose that energy is injected into the primordial plasma in the early universe. CMB photons are thermalized with the injected energy in the early epochs through interactions between photons and electrons, and the CMB spectrum maintains its blackbody spectrum. However, as the Universe expands and cools down, the time scales of these interactions become larger than the cosmological time scale. Therefore, the CMB spectrum cannot maintain the blackbody spectrum, and, instead, a deviation from the blackbody spectrum emerges. In the thermalization process of the CMB photons, the main interactions are Compton scattering, double Compton scattering, and bremsstrahlung. Accordingly, the evolution of the CMB spectrum is given by the Boltzmann equation with collision terms as [11,47,60]

$$\frac{\partial f}{\partial t} = C_{\rm K} + C_{\rm DC} + C_{\rm BR} + x\frac{\partial f}{\partial x}\frac{\partial}{\partial t}\left[\ln\left(\frac{T_e}{T_{\gamma 0}(1+z)}\right)\right], \tag{1}$$

where $T_{\gamma 0}$ is the CMB temperature at the present epoch, f is the distribution function of the CMB photons, and we introduce the dimensionless photon momentum (frequency), $x = p/T_e$ with the electron temperature T_e. The first three terms with the subscripts K, DC, and BR on the right-hand side represent the collision terms for Compton scattering, double Compton scattering, and bremsstrahlung, respectively.

The last term in Eq. (1) arises because the electron temperature evolves with time. The evolution of the electron temperature is

$$\frac{dT_e}{dt} = -2HT_e - \frac{4\sigma_{\rm T}\rho_\gamma}{3m_e f_*}\left(T_e - \frac{1}{\rho_\gamma \pi^2}\int dp\ p^4 f(1+f)\right), \tag{2}$$

where m_e is the electron mass, $\sigma_{\rm T}$ is the Thomson cross section, ρ_γ is the energy density of the CMB photons, and f_* includes the correction due to baryons, because baryons are quickly thermalized with electrons by Coulomb scattering. Here, $f_* = [(1+x_e)/2 - (3+2x_e)Y_p/8](1-Y_p/2)^{-1}/x_e$ with the ionization fraction of electrons x_e and the primordial helium mass fraction Y_p, and we set $Y_p = 0.25$ throughout the paper. In Eq. (2), the first term is due to the Hubble expansion and the second term represents the Compton cooling. The time scale of the Compton cooling is given by $t_{\rm CC} = 3m_e f_*/4\sigma_{\rm T}\rho_\gamma$. At redshift $z > 500$, because $t_{\rm CC} < t_{\rm H}$, where $t_{\rm H}$ is the Hubble time scale, the second term dominates over the first term on the right-hand side of Eq. (2). When the distribution function of the CMB photons is a blackbody spectrum with the temperature $T_\gamma = T_{\gamma 0}(1+z)$, the second term is proportional to $T_e - T_\gamma$. Therefore, when the electron temperature is tightly coupled with the CMB temperature, we obtain $T_e(z) = T_{\gamma 0}(1+z)$ and we can ignore the last term in Eq. (1).

2.1. *Compton scattering*

The Compton scattering term is described as it appears in the Kompaneets equation [66]:

$$C_{\rm K} = \dot{\tau}_{\rm C}\frac{T_e}{m_e}\frac{1}{x^2}\frac{\partial}{\partial x}x^4\left[\frac{\partial f}{\partial x} + f^2 + f\right], \tag{3}$$

where $\dot{\tau}_{\rm C} = x_e n_e \sigma_{\rm T}$ with the electron number density n_e.

In the brackets in Eq. (3), the first term represents the energy transfer due to the Doppler effect and the last two terms describe the recoil effects.

Although Compton scattering cannot change the number density of photons, it can redistribute the photon momenta. According to Ref. [25], the kinetic thermalization by Compton scattering is given by

$$t_{\rm K} = \frac{1}{4\dot{\tau}_{\rm C}}\frac{m_e}{T_e} = 1.23\times 10^{29}\,(1+z)^{-4}\left(\frac{h^2\Omega_B}{0.0226}\right)^{-1}\left(\frac{T_e}{T_\gamma}\right)^{-1}\ {\rm s}, \tag{4}$$

where $h = H_0/100$ and Ω_B is the energy density parameter of baryons.

2.2. *Double Compton scattering*

Double Compton scattering is one of the photon-creating processes, described by the reaction $\gamma + e^- \to \gamma + \gamma + e^-$. This corresponds to the lowest-order correction to Compton scattering. Double Compton scattering plays an important role in the thermalization of the CMB. In particular, it provides the dominant contribution in the evolution of the photon number density [26].

The double Compton scattering term in the Boltzmann equation is expressed as [70]

$$C_{\rm DC} = \dot{\tau}_{\rm C} \frac{4\alpha}{3\pi} \left(\frac{T_e}{m_e}\right)^2 \frac{g_{\rm DC}}{x^3} \left[1 - f(e^x - 1)\right], \tag{5}$$

where α is the fine structure constant and $g_{\rm DC}$ is the effective double Compton Gaunt factor. While $g_{\rm DC}$ drops exponentially in the limit of $x \gg 1$, in the limit of $x \ll 1$ it is given as

$$g_{\rm DC} \approx \int dx\, x^4 f(f+1). \tag{6}$$

More details about the double Compton Gaunt factor are discussed in Ref. [21]. Equation (5) tells us that double Compton scattering makes the CMB spectrum reach the blackbody spectrum with the temperature T_e. In particular, this effect is efficient at low frequencies.

According to Eq. (5), we define the time scale of double Compton scattering as

$$t_{\rm DC} = \frac{3\pi}{4\alpha\dot{\tau}_{\rm C}} \frac{x^3}{e^x - 1} I_{\rm BB}^{-1} \left(\frac{m_e}{T_e}\right)^2 = 1.34 \times 10^{40} \frac{x^3}{e^x - 1} (1+z)^{-5} \left(\frac{\Omega_B h^2}{0.0226}\right)^{-1} \left(\frac{T_e}{T_\gamma}\right)^{-2} \text{s}, \tag{7}$$

where $I_{\rm BB} = \int dx\, x^4 f_{\rm BB}(f_{\rm BB}+1)$ with a blackbody spectrum $f_{\rm BB}$.

2.3. *Bremsstrahlung*

Bremsstrahlung is also an important process for photon creation in the early universe. The expression for bremsstrahlung in the Boltzmann equation is given by [70]

$$C_{\rm BR} = \dot{\tau}_{\rm C} \frac{g_{\rm BR}}{e^x x^3} \left[1 - f(e^x - 1)\right] \frac{4\pi\alpha m_e^{1/2}}{(2\pi T_e)^{7/2}} \sum_i Z_i^2 n_i, \tag{8}$$

where $g_{\rm BR}$, Z_i, and N_i are respectively the bremsstrahlung Gaunt factor, the charge, and the number density for a nucleon of the atomic species i. The bremsstrahlung Gaunt factor can be approximated as

$$g_{\rm BR} = \begin{cases} \ln(2.25x), & x < 0.375 \\ \pi/\sqrt{3}, & x > 0.375. \end{cases} \tag{9}$$

In the case of fully ionized plasma, we can approximate the sum in Eq. (8) as

$$\sum_i Z_i^2 n_i = n_B, \tag{10}$$

where n_B is the number density of baryons. For a detailed expression of bremsstrahlung including the bremsstrahlung Gaunt factor, see Ref. [22].

Similar to the double Compton case, we define the time scale of bremsstrahlung as

$$t_{\rm BR} = \frac{(2\pi T_e)^{7/2}}{4\pi\alpha m_e^{1/2} n_B \dot{\tau}_{\rm C}} \frac{e^x}{g_{\rm BR}} \frac{x^3}{e^x - 1} = 8.59 \times 10^{26} \frac{x^3}{e^x - 1} (1+z)^{-5/2} \left(\frac{h^2\Omega_B}{0.0226}\right)^{-2} \left(\frac{T_e}{T_\gamma}\right)^{7/2} \text{s}. \tag{11}$$

Therefore, the photon-creation efficiency of bremsstrahlung depends on the cosmological parameters, redshifts, and photon frequency. Comparing Eqs. (7) and (11) for $h^2\Omega_b$ measured in our Universe, we can find that double Compton scattering happens to be the dominant effect in thermalization.

2.4. Comparison of time scales

The thermalization of CMB photons is achieved by three interactions: Compton scattering, double Compton scattering, and bremsstrahlung. In order to illustrate the steps of the CMB thermalization, let us compare the time scales of these interactions (for a more detailed discussion, see Ref. [47]).

Among these interactions, the time scale of kinetic thermalization due to Compton scattering is the smallest. As long as $t_{\rm K} < t_{\rm H}$, kinetic thermal equilibrium is established and the CMB spectrum is described as a Bose–Einstein distribution with a chemical potential. The decoupling epoch of the kinetic thermalization is obtained by solving $t_{\rm K} = t_{\rm H}$. The redshift at which this decoupling occurs, $z_{\rm K}$, is

$$z_{\rm K} \approx 4.7 \times 10^4 \left(\frac{h^2\Omega_B}{0.0226}\right)^{-1/2}. \tag{12}$$

At redshift $z < z_{\rm K}$, the kinetic thermalization of the CMB photons is not realized by Compton scattering. Although here we simply compare the time scales of kinetic thermalization and Hubble expansion, Burigana et al. numerically showed that a Bose–Einstein distribution is not established $z < z_{\rm fr}$ where [11]

$$z_{\rm fr} = 4\sqrt{2}z_{\rm K}. \tag{13}$$

We adopt $z_{\rm fr}$ as the freeze-out redshift of the Bose–Einstein distribution below which the injected energy is not thermalized.

Once a Bose–Einstein distribution is established, the spectrum starts to shift to a blackbody spectrum by the photon number change due to double Compton scattering and bremsstrahlung. Comparing the time scales of both interactions, double Compton scattering gives the dominant contribution above $z_{\rm DB}$:

$$z_{\rm DB} = 1.9 \times 10^5 \left(\frac{h^2\Omega_B}{0.0226}\right)^{2/5}. \tag{14}$$

The time scales of double Compton scattering and bremsstrahlung are frequency-dependent. Therefore, the decoupling epochs of these interactions also depend on the photon frequencies. At redshift z, the frequencies above which these interactions are decoupled are provided by

$$x_{H,\rm DC} \approx 6.0 \times 10^{-11}(1+z)^{3/2}\left(\frac{h^2\Omega_B}{0.0226}\right)^{1/2} \tag{15}$$

for double Compton scattering and

$$x_{H,\rm BR} \approx 2.3 \times 10^{-4}(1+z)^{5/4}\left(\frac{h^2\Omega_B}{0.0226}\right) \tag{16}$$

for bremsstrahlung in the limit of $x \ll 1$.

Since the time scale of the kinetic thermalization due to Compton scattering, $t_{\rm K}$, is frequency-independent, the frequency-dependent time scales for double Compton and bremsstrahlung become smaller at low frequencies. These critical frequencies, where these time scales are equal with $t_{\rm K}$, are given in the limit of $x \ll 1$ by

$$x_{c,\rm DC} \approx 3 \times 10^{-6}(1+z)^{1/2} \tag{17}$$

for double Compton scattering and

$$x_{c,\rm BR} \approx 1.2 \times 10(1+z)^{3/4} \tag{18}$$

for bremsstrahlung. We define the critical frequency as

$$x_c^2 = x_{c,\mathrm{DC}}^2 + x_{c,\mathrm{BR}}^2. \tag{19}$$

At frequencies lower than x_c, a blackbody spectrum is quickly established, while the distribution at higher frequencies is expressed by a Bose–Einstein distribution.

3. CMB spectral distortions

Once energy is injected in the early universe, it starts to be thermalized with the CMB photons by interactions between photons and electrons, depending on the energy injection epoch. The resultant CMB frequency spectrum is obtained by solving the Boltzmann equation numerically (see, e.g., Ref. [22] for recent work).

Conventionally, aside from the blackbody spectrum, the resultant spectrum is discussed in terms of the spectral distortions from a blackbody spectrum, which are classified into two types: μ-type distortion, in which the CMB spectrum is represented as a Bose–Einstein distribution with a frequency-dependent chemical potential, and y-type distortion, in which the spectral distortion is parametrized by the Compton y-parameter. These distortions can be described by simple analytic expressions in some limits. In this section, we review these distortions analytically, including the third type of CMB distortion, i-type distortion, which describes an intermediate distortion between the μ-type and the y-type [59,61].

3.1. μ-type distortion

When the time scale of the kinetic thermalization due to Compton scattering is smaller than the cosmological time scale, $z > z_{\mathrm{K}}$, the distribution of the CMB reaches kinetic equilibrium with the electron temperature. Although double Compton scattering and bremsstrahlung could change the photon number at low frequencies, the photon number is conserved at high frequencies where double Compton scattering and bremsstrahlung are inefficient. Therefore, a blackbody spectrum cannot be established. Instead, such a kinetic equilibrium is described as a Bose–Einstein distribution with a frequency-dependent chemical potential $\mu(x)$:

$$f_{\mathrm{BE}} = \frac{1}{e^{x+\mu(x)} - 1}. \tag{20}$$

Compared to a blackbody spectrum with the same temperature, a Bose–Einstein distribution with a positive chemical potential has fewer photons. On the other hand, the spectrum with a negative chemical potential has more photons (see Fig. 1).

The chemical potential depends on the injected energy. In order to evaluate this dependence, we parametrize the energy injection by the relative number density of photons, $\delta n_\gamma / n_\gamma$, and the relative energy density, $\delta \rho_\gamma / \rho_\gamma$ [47]. For simplicity, we assume that the chemical potential μ is not frequency-dependent in what follows.

We consider energy injection into the CMB with the temperature T_i at $z > z_{\mathrm{K}}$. As discussed in the previous section, a Bose–Einstein distribution of photons is established, which is kinetically thermalized with electrons with a temperature T_e. We can write the energy and the number densities in a Bose–Einstein distribution as

$$\rho_{\mathrm{BE}} = \frac{1}{\pi^2} \int f_{\mathrm{BE}} p^3 dp = \rho_{\mathrm{BB}}(T_e) \psi(\mu), \tag{21}$$

and

$$n_{\mathrm{BE}} = \frac{1}{\pi^2} \int f_{\mathrm{BE}} p^2 dp = n_{\mathrm{BB}}(T_e) \phi(\mu), \tag{22}$$

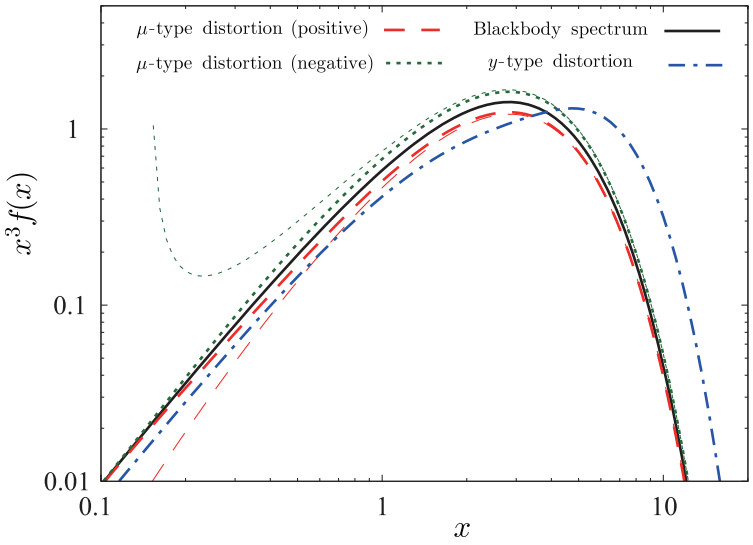

Fig. 1. μ-type and y-type distortions. The red (dashed) and green (dotted) lines represent μ-type distortions with a negative and positive chemical potential, respectively. The blue (dot-dashed) line is for the y-type distortion. For comparison, the blackbody spectrum with the same temperature is plotted as the black (solid) line. The thin lines show the spectra in the Bose–Einstein distributions with constant chemical potentials.

where $\rho_{\rm BB}(T_e)$ and $n_{\rm BB}(T_e)$ are the energy and number densities in the blackbody distribution with the temperature T_e. In these equations, ψ and ϕ represent the corrections of the Bose–Einstein distribution from the blackbody spectrum. In the limit of $\mu \ll 1$, these are given by

$$\psi(\mu) = 1 - 3\frac{I_2}{I_3}\mu, \tag{23}$$

and

$$\phi(\mu) = 1 - 2\frac{I_1}{I_2}\mu, \tag{24}$$

where I_n is defined as

$$I_n \equiv \int dx \frac{x^n}{e^x - 1} = n!\zeta(n+1). \tag{25}$$

Taking into account the conservation of the energy and the number densities before and after the kinetic equilibrium, we obtain

$$\rho_{\rm BE} = \rho_{\rm BB}(T_i)\left(1 + \frac{\delta\rho_\gamma}{\rho_\gamma}\right), \tag{26}$$

and

$$n_{\rm BE} = n_{\rm BB}(T_i)\left(1 + \frac{\delta n_\gamma}{n_\gamma}\right). \tag{27}$$

Using Eqs. (21) and (22), we can solve Eqs. (26) and (27) for the chemical potential μ. Up to the first order of μ, $\delta\rho_\gamma/\rho_\gamma$ and $\delta n_\gamma/n_\gamma$, we obtain

$$\mu = \left(8\frac{I_1}{I_2} - 9\frac{I_2}{I_3}\right)^{-1}\left(3\frac{\delta\rho_\gamma}{\rho_\gamma} - 4\frac{\delta n_\gamma}{n_\gamma}\right), \tag{28}$$

where $8I_1/I_2 - 9I_2/I_3$ is roughly 2.143. The resultant chemical potential depends on the total number and energy densities of the injected photons, and is independent of these spectra.

Equation (28) shows that, when the injection is parametrized by only energy density with zero number density of injected photons, the chemical potential is positive. This is because the energy

injection first heats up the electrons as $T_e > T_i$, and these electrons tend to make the CMB spectrum a blackbody spectrum with T_e. However, the photon number density is conserved and proportional to T_i^3. This number density is lower than that of the new blackbody spectrum with T_e. Therefore, the chemical potential arises due to the gap between these number densities. When the energy injection is in photons ($\delta n_\gamma/n_\gamma \neq 0$), this additional number density of photons compensates for this gap and reduces the chemical potential in Eq. (28).

As seen in the previous section, double Compton scattering and bremsstrahlung are efficient at low frequencies. Therefore, one can expect that a blackbody distribution can be established at these frequencies. This dependence brings a frequency-dependent chemical potential. The analytic approximation form for the chemical potential evolution is obtained in two limits: the low-frequency limit and the high-frequency limit.

In the low-frequency limit, since double Compton scattering and bremsstrahlung lead a blackbody distribution instantaneously, we can assume that the steady state approximation of the Boltzmann equation is valid[1]:

$$\frac{\partial f}{\partial t} = C_K + C_{\rm BR} + C_{\rm DC} \approx 0. \tag{29}$$

This approximation provides

$$\frac{1}{x}\frac{d}{dx}\left[x^4 \frac{\exp\left[x+\mu(x)\right]}{\left(\exp\left[x+\mu(x)\right]-1\right)^2}\frac{d\mu}{dx}\right] = 4x_c^2 \frac{e^x}{x^3}\frac{\exp(\mu)-1}{\exp\left[x+\mu\right]-1}. \tag{30}$$

In the case of $\mu \ll x$, the solution of Eq. (30) is given by [26,113]

$$\mu(x) = \mu_c \exp\left[-2x_c/x\right], \tag{31}$$

where μ_c is the chemical potential in the high-frequency limit, $x \gg 1$. The chemical potential exponentially drops at low frequencies, as we expect, and its amplitude depends on the evolution of the chemical potential at high frequencies, μ_c. Recently, a more precise analytic form was discussed in Ref. [60].

Now we consider the evolution of chemical potential at high frequencies. Equation (31) suggests that the chemical potential is constant in the limit of $x \gg x_c$. For simplicity, we assume that the energy injection generates the chemical potential μ at high frequencies.

The evolution of the number and energy densities of photons with chemical potential is rewritten as:

$$\frac{1}{n_{\rm BE}}\frac{dn_{\rm BE}}{dt} = \frac{1}{n_{\rm BB}}\frac{dn_{\rm BB}}{dT_e}\frac{dT_e}{dt} + \frac{1}{\phi}\frac{d\phi}{d\mu}\frac{d\mu}{dt}, \tag{32}$$

$$\frac{1}{\rho_{\rm BE}}\frac{d\rho_{\rm BE}}{dt} = \frac{1}{\rho_{\rm BB}}\frac{d\rho_{\rm BB}}{dT_e}\frac{dT_e}{dt} + \frac{1}{\psi}\frac{d\psi}{d\mu}\frac{d\mu}{dt} = 0. \tag{33}$$

From these equations, we obtain

$$\frac{d\mu}{dt} = -\frac{1}{B(\mu)}\left(\frac{4}{n_{\rm BE}}\frac{dn_{\rm BE}}{dt}\right), \tag{34}$$

where

$$B(\mu) = 3\frac{d\ln\psi(\mu)}{d\mu} - 4\frac{d\ln\phi(\mu)}{d\mu}. \tag{35}$$

[1] This is valid over all x, when $z > z_{\rm K}$.

From the Boltzmann equation, the evolution of the number density is also given by

$$\frac{1}{n_{\rm BE}}\frac{dn_{\rm BE}}{dt}=\frac{1}{I_2\phi(\mu)}\left(\frac{I_{\rm BE}}{I_{\rm BB}}\frac{J_{\rm DC}}{t_{\rm DC}}+\frac{J_{\rm BR}}{t_{\rm BR}}\right), \tag{36}$$

where

$$I_{\rm BE}=\int dx x^4(1+f_{\rm BE})f_{\rm BE}=4I_3\phi(\mu), \tag{37}$$

and

$$J_{\rm DC}=\int dx\, x^2\left[\frac{1}{e^x-1}-f\right],\quad J_{\rm BR}=\int dx\, x^2\left[\frac{1}{e^x-1}-f\right]. \tag{38}$$

Accordingly, the evolution of the chemical potential is approximately provided as

$$\frac{d\mu}{dt}=-\frac{\mu}{t_{\mu,{\rm i}}}. \tag{39}$$

Here i denotes DC for $t_{\mu,{\rm DC}}<t_{\mu,{\rm BR}}$, otherwise i is BR, where $t_{\mu,{\rm i}}$ is expressed as

$$t_{\mu,{\rm i}}=\frac{1}{2}BI_2\frac{t_{\rm K}}{x_{{\rm c,i}}}. \tag{40}$$

Equation (39) suggests that the chemical potential exponentially decreases by the change of the number density due to double Compton scattering and bremsstrahlung.

Taking into account the relation between the energy injection and the resultant chemical potential (Eq. (28)), Hu et al. provided the evolution equation for the chemical potential with energy injection as [49]

$$\frac{d\mu}{dt}\approx-\frac{\mu}{t_{\mu,{\rm i}}}+1.4\frac{d}{dt}\frac{Q}{\rho_\gamma}, \tag{41}$$

where Q is the injected energy density and Q/ρ_γ is the fractional energy injection. For example, in the limit of double Compton scattering domination, the solution of this equation is given by

$$\mu=1.4\int_\infty^{z_{\rm fr}}dz\left(\frac{d}{dz}\frac{Q}{\rho_\gamma}\right)\exp\left[-\left(\frac{z}{z_{\mu,{\rm DC}}}\right)^{5/2}\right], \tag{42}$$

where $z_{\rm fr}$ is the freeze-out redshift of a Bose–Einstein distribution given by Eq. (13) and $z_{\mu,{\rm DC}}$ is the redshift corresponding to $t_{\mu,{\rm DC}}$, $z_{\mu,{\rm DC}}\approx 2.6\times10^6(h^2\Omega_b/0.0226)$.

3.2. *y-type distortion*

For $z<z_{\rm K}$, the injected energy cannot be thermalized with the CMB photons. However, through the Compton cooling term in Eq. (2), the injected energy can increase the electron temperature efficiently if the energy injection occurs at $z>500$.

Even if $z<z_{\rm K}$, some fraction of Compton scattering with energy transfer between electrons and CMB photons is expected. Heated electrons upscatter the CMB photons. As a result, the CMB spectrum deviates from the blackbody spectrum, and this type of distortion is called y-type distortion. Although the exact shape of the CMB spectrum is obtained by numerical calculation of the Boltzmann equation, the simple analytical form can be obtained in two limits: the high electron temperature limit, $T_e\gg T_\gamma$, and the strong Compton cooling limit, $t_{\rm CC}\ll t_{\rm H}$.

Let us consider the case where the electron temperature is strongly heated: $T_e\gg T$. Because we consider $z<z_{\rm K}$, we can ignore $C_{\rm DC}$ and $C_{\rm BR}$, and Eq. (1) provides the original Kompaneets equation.

We assume that the optical depth of Compton scattering is low. In this condition, a CMB photon is scattered only once. Therefore, we can ignore the recoil term, and Eq. (1) finally yields

$$\frac{\partial f}{\partial y} = \frac{1}{x}\frac{\partial}{\partial x}\left(x^4 \frac{\partial f}{\partial x}\right), \tag{43}$$

where y is the dimensionless Compton y-parameter, which corresponds to the optical depth for the energy transfer through Compton scattering:

$$y = \int dt\, x_e n_e \sigma_{\rm T} \frac{T_e}{m_e}. \tag{44}$$

The solution of Eq. (43) is easily obtained in the limit that the deviation from the blackbody spectrum is very small, $f = f_{\rm BB} + \delta f$ with $|\delta f| \ll f_{\rm BB}$. In this limit, the distortion of the spectrum is expressed as a y-type distortion [133]:

$$\frac{\delta f}{f_{\rm BB}} = y \frac{x e^x}{e^x - 1}\left[x\left(\frac{e^x + 1}{e^x - 1} - 4\right)\right]. \tag{45}$$

At low frequencies, namely, in the limit of the Rayleigh–Jeans, Eq. (45) is approximated to $\delta f / f_{\rm BB} = \delta T / T|_{\rm RJ} \approx -2y$. This means that CMB photons at low frequencies are upscattered and the resultant deficits of the spectrum arise at these frequencies. On the other hand, Eq. (45) shows that the sign becomes positive beyond the peak of the CMB spectrum. This reflects the fact that the upscattering from low frequencies causes the excess of photons from the blackbody spectrum at high frequencies.

The optical depth of the energy transfer by Compton scattering is proportional to T_e. Therefore, y-type distortions are generated easily where the electron temperature is high. One can find such high-temperature electrons inside clusters of galaxies where the electron temperature reaches about 10 keV. The y-type distortion produced by hot electrons in clusters of galaxies is called the "Sunyaev–Zel'dovich effect" [112], and has been studied (for a review, see Ref. [8]). We consider other cosmological sources to heat electrons in the early universe in Sect. 5.

Next we consider the Compton cooling limit, $t_{\rm CC} < t_{\rm H}$. In this limit, CMB photons are strongly coupled with electrons and the difference between T_e and $T_{\rm CMB}$ is small, as expected from Eq. (2). In this case, we cannot ignore the recoil term of the Compton term. However, when the spectral deviation from the blackbody is very small, we can solve the Kompaneets equation iteratively. The blackbody spectrum with the temperature T_γ satisfies $f_{\rm BB} + f_{\rm BB}^2 = -(\partial f/\partial p) T_\gamma$. Applying this equation to the Compton scattering term, we can obtain the same form as in Eq. (43) in this small distortion limit when we rewrite the y-parameter as

$$y = \int dt\, x_e n_e \sigma_{\rm T} \frac{T_e - T}{m_e}, \tag{46}$$

instead of Eq. (44).

Up to now, we have considered y-type distortion as a result of scattering with electrons. However, y-type distortion also arises in mixing of blackbody spectra with different temperatures [63,132]. We consider temperature fluctuations $T + \Delta T$ with the average temperature T and non-zero $\langle \Delta T^2 \rangle$ (and $\langle \Delta T \rangle = 0$), where $\langle\ \rangle$ denotes the average. At each spatial point, the CMB spectrum is expressed in the blackbody spectrum with a fluctuating temperature $T + \Delta T$. Keeping the terms up to the second

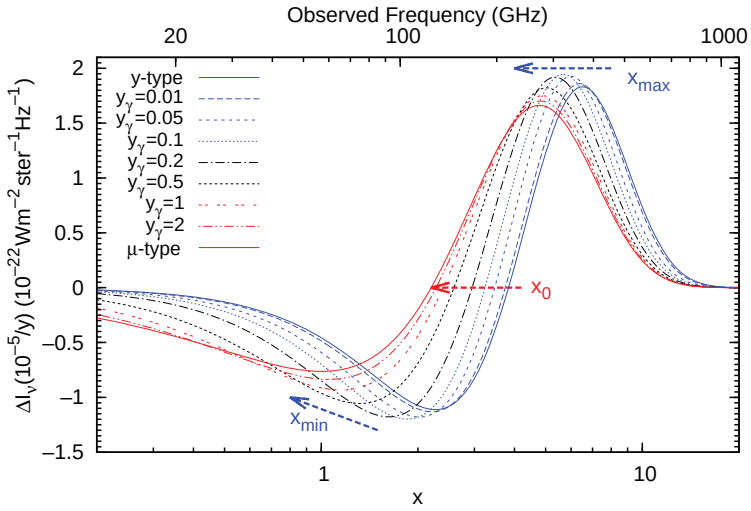

Fig. 2. i-type distortion. As y_γ increases, i-type distortions shift from a y-type distortion to a μ-type distortion. This figure is taken from Ref. [59].

order in $\Delta T/T$ and taking the average of the CMB spectrum gives [63]

$$\langle f_{\rm BB}(T+\Delta T)\rangle \approx f_{\rm BB}(T_{\rm new}) + \frac{1}{2} f_{\rm BB}(T) \left\langle \left(\frac{\Delta T}{T}\right)^2 \right\rangle \frac{x e^x}{e^x-1} \left[x \left(\frac{e^x+1}{e^x-1} - 4 \right) \right], \tag{47}$$

where $T_{\rm new} = T[1 + \langle (\Delta T/T)^2 \rangle]$. Therefore, mixing the blackbody spectra gives a blackbody spectrum with temperature $T_{\rm new}$ with y-type distortions whose y-parameter is given by

$$y = \frac{1}{2} \left\langle \left(\frac{\Delta T}{T}\right)^2 \right\rangle. \tag{48}$$

This result tells us that y-type distortion can be created by a superposition of blackbody spectra or averaging the small-scale temperature fluctuations, even if there is no Compton scattering.

3.3. *i-type distortion*

Below $z_{\rm fr}$, a Bose–Einstein distribution of CMB photons with energy injection cannot be maintained. However, some Compton scatterings are still expected and the kinetic equilibrium with electrons is partially established. The distortion in this regime can be described by neither μ- nor y-type distortions; it is the intermediate type, called i-type distortion [59,61]. This regime corresponds to the redshifts between $z = 1.5 \times 10^4$ and 2×10^5.

The i-type distortions have been studied numerically [59]. In Ref. [59], the i-distortion is labeled by y_γ:

$$y_\gamma(z) = -\int_{z_{\rm in}}^{z} \frac{dz}{(1+z)H} \frac{1}{\dot\tau_{\rm C}} \frac{T_e}{m_e}, \tag{49}$$

where $z_{\rm in}$ is the redshift at which energy is injected. Figure 2 shows the i-type distortions as the intensity difference from a blackbody spectrum. An increase in y_γ indicates an increase in the optical depth of Compton scattering. Therefore, as y_γ increases, the spectral distortion shifts from a y-type distortion to a μ-distortion via i-type distortions. In particular, the zero point, which is defined as the point x_0 where $f(x_0) = f_{\rm BB}(x_0)$, monotonically moves from the value of a y-type distortion to that of a μ-type distortion.

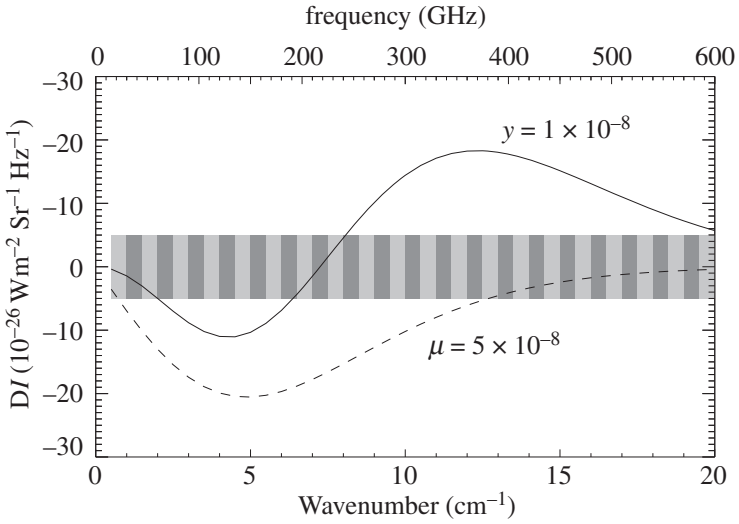

Fig. 3. PIXIE instrumental noise in each synthesized frequency channel. The solid and dashed lines represent y-type and μ-type distortions, respectively. PIXIE can detect these distortions at the 5σ level. The figure is taken from Ref. [65].

One of the interesting applications of i-type distortions is for spectral distortions due to Silk damping, which we discuss in Sect. 5.1. Measurement of i-type distortions, in combination with μ-type distortions, provides a way to lift the degeneracy between the amplitude and the spectral index of the primordial power spectrum [61].

4. Observational constraints on CMB distortions

Since Penzias and Wilson's discovery of the CMB [91], there have been many attempts to measure the CMB spectrum and detect distortions from a blackbody spectrum. Among them, the FIRAS instrument on-board on the COBE satellite measured the "mean" frequency spectrum over a wide range of frequencies [31,74]. The observed data are consistent with a blackbody spectrum and no CMB distortions are detected within the sensitivity of COBE/FIRAS[2], providing a stringent constraint on both μ-type and y-type distortions.

At the moment, two projects aiming for detection of the CMB distortions, PIXIE [65] and PRISM [96], are proposed. Their sensitivities are 10^3–10^4 times better than that of COBE/FIRAS. Hence, it is highly expected that these experiments will be able to detect CMB distortions or at least provide much stringer constraints.

In this section, we summarize the current status of constraints on CMB distortions and give an overview of future projects for precise measurement of the CMB distortions.

4.1. Current constraints

The COBE Far Infrared Absolute Spectrophotometer (FIRAS) was a rapid-scan polarizing Michelson interferometer on the COBE satellite. It was designed to measure the spectrum of the CMB and to detect the deviation of the observed spectrum from the blackbody spectrum. COBE/FIRAS scanned

[2] Here we mention the homogeneous component of CMB distortions. Local CMB distortions have already been detected as y-type distortions due to galaxy clusters, i.e., Sunyaev–Zel'dovich effects. See Ref. [8] and references therein.

the full sky with 7° angular resolution and its frequency range was from 1 cm^{-1} to 95 cm^{-1}, divided into two parts, the high- and low-frequency channels, at 20 cm^{-1}. The first result was reported by Mather et al. [75], using the low-frequency data at high Galactic latitudes collected in the first 9 minutes of the mission. The result showed that the deviation from a blackbody is less than 1% of the peak intensity. Later, the final result was released [31], based on 10 months' worth of low-frequency data. The CMB temperature has been measured to be 2.728 ± 0.004 K at 95% confindence level. Distortion from the blackbody spectrum was not detected and the limits on the distortion were given as

$$|y| < 1.5 \times 10^{-5}, \tag{50}$$

and

$$|\mu| < 9.0 \times 10^{-5}, \tag{51}$$

at 95% confidence level.

After COBE/FIRAS, several observations were performed to measure the absolute CMB frequency spectrum at lower frequencies than COBE/FIRAS.

The TRIS is a set of three absolute radiometers installed at Campo Imperatore in Italy. The TRIS operated between 1996 and 2000 and its radiometers were tuned at 0.60 (0.02 cm^{-1}), 0.82 (0.027 cm^{-1}), and 2.5 GHz (0.083 cm^{-1}) [101]. The TRIS has set the limit on the chemical potential distortion at 1 GHz, $|\mu| < 6 \times 10^{-5}$ at 95% confidence level [35].

The Absolute Radiometer for Cosmology, Astrophysics, and Diffuse Emission (ARCADE) is a balloon-borne instrument that consists of a set of 7 precision radiometers [32,105]. ARCADE had a successful flight in 2006, measuring the CMB frequency spectrum between 3 and 90 GHz (0.1 cm^{-1} and 3.0 cm^{-1}). Using these data, ARCADE set the 2σ upper limit on the μ-type distortion, $\mu < 6 \times 10^{-4}$ [101].

4.2. Future observations

Recently, two missions have been proposed in order to measure the absolute frequency spectrum: the Primordial Inflation Explorer (PIXIE) [65] and the Polarized Radiation Imaging and Spectroscopy Mission (PRISM) [96]. Although the primary aim of both missions is to measure (or constrain) the CMB polarization induced by gravitational waves produced during the inflationary epoch, they can measure the absolute CMB frequency spectrum and are expected to improve the constraints on CMB distortions.

PIXIE is a NASA Explorer-class mission [65]. The instrument consists of a polarizing Michelson interferometer configured as a nulling polarimeter. PIXIE will map the absolute CMB intensity in frequencies from 30 GHz to 6 THz (1 cm^{-1} to 50 m^{-1}) by 400 spectral channels of 15 GHz bandwidths. The instrument sensitivity of PIXIE to the unpolarized signal will be designed as

$$\Delta I = 5 \times 10^{-26}\,\mathrm{Wm}^{-2}\,\mathrm{Sr}^{-1}\,\mathrm{Hz}^{-1} \tag{52}$$

in each frequency bin. This sensitivity enables detection of the distortions with $\mu = 5 \times 10^{-8}$ or $y = 1.0 \times 10^{-8}$ at the 5σ level (see also Fig. 3).

PRISM was proposed to ESA as a large-class mission [96]. PRISM will consist of two instruments. One of them is a lower angular resolution spectrometer that will measure the absolute sky emission over 30 GHz to 6 THz (1 cm^{-1} to 50 m^{-1}), similar to PIXIE. In particular, the sensitivity

at frequencies lower than 600 GHz reaches

$$\Delta I = 6 \times 10^{-27}\,\mathrm{Wm^{-2}\,Sr^{-1}\,Hz^{-1}} \tag{53}$$

in the current design. This sensitivity is better than PIXIE. Therefore, PRISM is expected to be sensitive to μ-type and y-type distortions at the level of few $\times 10^{-9}$.

4.3. Measurement of distortion anisotropies

So far, we have discussed the measurement of CMB distortions that are isotropic in the sky. However, anisotropies of CMB distortions arise, depending on the spatial fluctuations in the source distributions of the distortions. Such anisotropies include the Sunyaev–Zel'dovich effect due to clusters of galaxies.

PIXIE can measure these anisotropies by using the beam width $\theta_b = 1.6^\circ$. Its 1σ uncertainties in the μ and y parameters averaged over the full sky are $\delta\mu = 10^{-8}$ and $\delta y = 2 \times 10^{-9}$, respectively, and this sensitivity provides the noise angular power spectrum as

$$C_l^{\mu\mu,N} = 1.3 \times 10^{-15} \times \exp\left(\frac{l^2}{l_{\mathrm{max}}^2}\right) \tag{54}$$

for a μ-type distortion and

$$C_l^{yy,N} = 5.0 \times 10^{-17} \times \exp\left(\frac{l^2}{l_{\mathrm{max}}^2}\right) \tag{55}$$

for a y-type distortion.

The anisotropies of the distortions can be observed as the CMB temperature anisotropy

$$\frac{\delta T}{T} \approx -\frac{\delta\mu}{x} \tag{56}$$

for a μ-type distortion and

$$\frac{\delta T}{T} \approx \left(x\frac{e^x+1}{e^x-1} - 4\right) y \tag{57}$$

for a y-type distortion. Since these temperature anisotropies have frequency dependence, measuring the temperature anisotropies in multiple frequency channels allows us to find the anisotropies of the distortions. Therefore, although homogeneous CMB distortions can be measured only by absolutely calibrated experiments such as PIXIE and PRISM, the anisotropies of CMB distortions can be probed not only by absolutely calibrated experiments but also relatively calibrated experiments like Planck [34]. The experimental noise power spectrum for a relatively calibrated experiment using two different frequency channels ν_1 and ν_2 is expressed by

$$C_l^{\mu\mu,N} = \left[\frac{\nu_1\nu_2/(\nu_1-\nu_2)}{56.80\,\mathrm{GHz}}\right]^2 \sum_{i=1,2} \sigma_{N,i}^2 \theta_{b,i}^2 b_{i,l}^{-2} \tag{58}$$

for a μ-type distortion and

$$C_l^{yy,N} = \left(\frac{1}{a(\nu_1)-a(\nu_2)}\right)^2 \sum_{i=1,2} \sigma_{N,i}^2 \theta_{b,i}^2 b_{i,l}^{-2} \tag{59}$$

for a y-type distortion, where the subscript i stands for 1 and 2, $\sigma_{N,i}$ is the 1σ uncertainty in $\delta T/T$ per pixel at frequency ν_i, $\theta_{b,i}$ is the beam width of channel ν_i, and $b_{i,l} = \exp\left(-l^2\theta_{b,i}^2/16\ln 2\right)$.

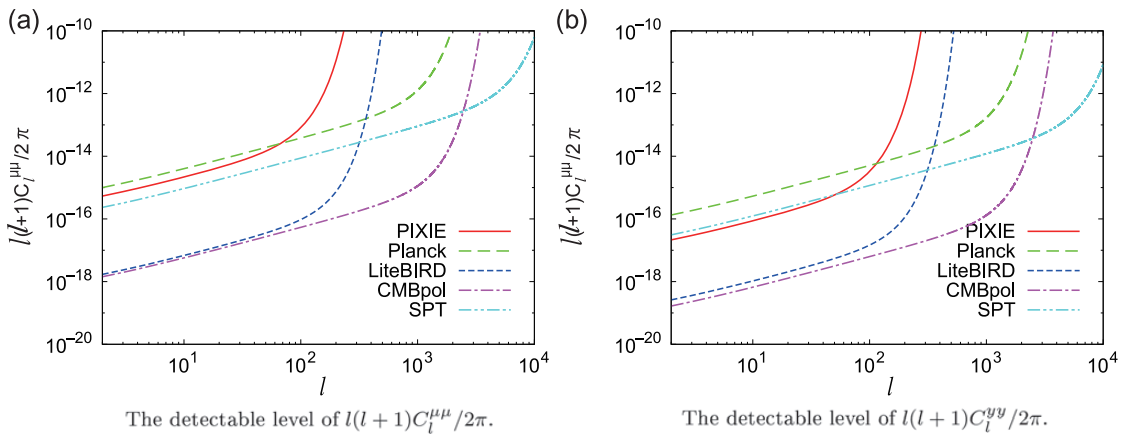

Fig. 4. The detectable levels of $l(l+1)C_l^{\mu\mu}/2\pi$ and $l(l+1)C_l^{yy}/2\pi$ in PIXIE (red solid), Planck (green long-dashed), LiteBIRD (blue short-dashed), CMBpol (magenta chain), and SPT (light blue two-dot chain). The figure is adapted from Ref. [80].

Table 1. Parameters for relatively calibrated experiments. θ_{bi} and σ_{Ni} are the Gaussian beam width at FWHM and temperature noise at frequency ν_i. Note that each satellite has some frequency bands other than those shown above. We have chosen the two bands that realize the best sensitivities.

	ν_1 [GHz]	θ_{b1}	σ_{N1}	ν_2 [GHz]	θ_{b2}	σ_{N2}
Planck	100	$9.5'$	2.5×10^{-6}	143	$7.1'$	2.2×10^{-6}
LiteBIRD	90	$60'$	2.1×10^{-8}	150	$36'$	3.3×10^{-8}
CMBpol	100	$8'$	1.1×10^{-7}	150	$5'$	1.6×10^{-7}
SPT	95	$1.7'$	9.6×10^{-6}	150	$1.2'$	5.5×10^{-6}

Miyamoto et al. have studied the experimental noise power spectra of the two ongoing projects, Planck [122] and SPT [97,97], and the two proposed projects, LiteBIRD [45] and CMBpol [6], as typical noise power spectra [80]. SPT is a ground-based telescope that focuses on the small-scale anisotropies compared with Planck. LiteBIRD is planed to have a better sensitivity per pixel than Planck, although its angular resolution is lower. CMBpol is a future CMB satellite with a sensitivity similar to LiteBIRD, and an angular resolution better than Planck. Figure 4 shows the detectable level of distortion anisotropies. The frequencies, beam widths, and sensitivities used in Fig. 4 are summarized in Table 1, where the frequencies are chosen from the observational frequencies for which the best sensitivity is realized.

5. Constraint on energy injection sources

As discussed in Sect. 3, energy injection in the early universe produces CMB spectral distortions. The type of distortion depends on the epoch at which the energy injection occurs. Therefore, measurement and constraints on CMB distortions provide a probe for physics related to the thermal history of the Universe. In this section, we review possible sources that create the CMB distortions in the early universe. Mainly, we review their current and prospective constraints.

5.1. Dissipation of acoustic waves

In the early universe, photons are tightly coupled with electrons via Thomson scattering and it can be assumed that the photon–baryon fluid is a single fluid [90]. Since the fluid has non-negligible

pressure due to photons, the density fluctuations cannot collapse gravitationally, and, instead, create acoustic waves with a sound speed of typically $1/\sqrt{3}$.

However, as the universe expands and cools, the plasma recombines, the coupling between photons and electrons becomes weak, and the photon mean free path due to the Thomson scattering increases. In other words, the diffusion scale of photons grows with time. Since acoustic waves lead to temperature fluctuations, the diffusion of photons between different phases of the acoustic waves mixes different temperatures [63]. In a macroscopic view, the dissipation of the acoustic waves occurs due to the shear viscosity and the heat conduction of the baryon–photon fluid [125]. This damping is well known as Silk damping [104]. Acoustic waves with wavelengths below the Silk scale cannot survive. The Silk damping scale grows with time. At the epoch of recombination, the Silk damping scale is roughly 8 Mpc.

In particular, in inflationary cosmology, a nearly scale-invariant spectrum of primordial curvature perturbations is predicted over a wide range of scales (from the horizon scale at the end of the inflationary epoch to scales larger than the current horizon scale) [37,40,81,108]. Therefore, the acoustic wave dissipation due to Silk damping is one of the promising energy release mechanisms to generate CMB distortions.

The CMB distortions due to Silk damping have been studied by many authors [4,20,24,46,111]. Recently, considering the second-order perturbation equations for CMB distortions, Chluba et al. showed that, while 2/3 of the dissipation energy is used to increase the blackbody temperature, the rest of the dissipation energy creates the CMB distortions [20]. Accordingly, the energy injection rate for the CMB distortions is given by

$$\frac{1}{a^4\rho_\gamma}\frac{d\,a^4Q}{dz} = -\frac{\dot{\tau}_{\rm C}}{(1+z)H(z)}\left[\frac{(3\Theta_1 - v_b)^2}{3} + \frac{9}{2}\Theta_2^2 - \frac{1}{2}\Theta_2\left(\Theta_2^{\rm P} + \Theta_0^{\rm P}\right) + \sum_{l\geq 3}(2l+1)\Theta_l^2\right], \tag{60}$$

where v_b is the Fourier component of the baryon velocity, and Θ_l and $\Theta_l^{\rm P}$ are, respectively, the lth multipole components of the temperature and the polarization fields. For example, Θ_l is defined as

$$\Theta_l(k) \equiv \frac{1}{2(-i)^l}\int_{-1}^{1} d\mu\; P_l(\mu)\Theta(k,\mu), \tag{61}$$

where $P_l(\mu)$ is the Legendre polynomial, $\Theta(k,\mu)$ is the Fourier component of the temperature fluctuations $\delta T/T$, and μ is $\hat{k}\cdot\hat{n}$ with the photon propagation direction $\hat{n}$. The multipole component of the polarization, $\Theta_l^{\rm P}$, is defined in the same way as Θ_l.

We can obtain Θ_l and v_b in Eq. (60) by solving the Boltzmann equations of photons and baryons numerically. However, the analytic approximations can be found in the limit of the tight coupling, $k/\dot{\tau}_{\rm C} \ll 1$ (see e.g. Ref. [28]), which is valid on scales where the energy of the acoustic waves is dissipated efficiently. In the limit of the tight coupling, we obtain

$$v_b \approx \frac{3\Theta_1}{1 - ikc_{\rm s}R/\dot{\tau}_{\rm C}}, \quad \Theta_2 \approx i\frac{4k}{9\dot{\tau}_{\rm C}}\Theta_1, \quad \Theta_2^{\rm P} + \Theta_0^{\rm P} \approx \frac{3}{2}, \quad \Theta_l \approx 0 \text{ for } l > 3, \tag{62}$$

where $R = 3\rho_b/(4\rho_\gamma)$ is the baryon-to-photon energy density ratio and $c_{\rm s}$ is the sound speed of the photon–baryon fluid, $c_{\rm s} = 1/\sqrt{3(1+R)}$.

The dipole component is related to the initial monopole component Θ_0. Taking into account the Silk damping, we can write

$$|\Theta_1|^2 \approx \frac{3\sin^2(kr_s)}{(1+R)}\Theta_0^2 e^{-2k^2/k_D^2}, \tag{63}$$

where r_s is the sound horizon, k_D is the diffusion scale given by

$$\frac{1}{k_D^2} = \int_z^\infty dz \frac{(1+z)}{6H(1+R)n_e\sigma_T}\left(\frac{R^2}{1+R}+\frac{16}{15}\right), \tag{64}$$

and we neglect the contributions of any metric perturbations.

The initial monopole component can be written in terms of the primordial curvature perturbations, $P_{\mathcal{R}}(k)$ [73]:

$$\Theta_0^2 = \frac{\alpha_\nu}{9}P_{\mathcal{R}}(k). \tag{65}$$

Here α_ν is defined as $\alpha_\nu = 4/[(2/5R_\nu)+(3/2)]^2$, where $R_\nu = \rho_\nu/(\rho_\gamma+\rho_\nu)$ with the neutrino energy density ρ_ν.

Therefore, we finally obtain the energy injection rate for CMB distortions as

$$\frac{1}{a^4\rho_\gamma}\frac{d\,a^4Q}{dz} \approx \frac{4\alpha_\nu c_s^2}{3\dot{\tau}_C(1+R)}\left(\frac{R^2}{1+R}+\frac{16}{15}\right)\int\frac{d^3k}{(2\pi)^3}k^2P_{\mathcal{R}}(k)\sin^2(kr_s)e^{-2k^2/k_D^2}. \tag{66}$$

This result tells us that the energy injection depends on the primordial curvature perturbations and the scale at which the energy dissipates efficiently corresponds to the Silk scale k_D. Hence, depending on the type of CMB distortions, the scale of the primordial perturbations, which can contribute to the CMB distortion, is different. μ-type distortion is sensitive to the power spectrum between $k \sim 10\,\mathrm{Mpc}^{-1}$ and $10^4\,\mathrm{Mpc}^{-1}$, while y-type distortion depends on the spectrum at $k \lesssim 10\,\mathrm{Mpc}^{-1}$. The measurement of the CMB distortions can probe the primordial curvature perturbations on small scales that we cannot access by CMB anisotropy observations and galaxy surveys.

The primordial curvature perturbations are parametrized as [67]

$$P_{\mathcal{R}} = \frac{2\pi^2\Delta_{\mathcal{R}}^2(k_0)}{k^3}\left(\frac{k}{k_0}\right)^{n_s-1+\frac{1}{2}\alpha_s\ln(\frac{k}{k_0})}, \tag{67}$$

with the normalized amplitude $\Delta_{\mathcal{R}}^2$, the pivot scale k_0, the spectral index n_s, and the running of the spectral index α_s. The best-fit parameters of the Wilkinson Microwave Anisotropy Probe (WMAP) 9-year data are $\Delta_{\mathcal{R}}^2(k_0) = 2.41 \pm 0.10 \times 10^{-9}$ and $n_s = 0.972 \pm 0.013$ at $k_0 = 0.002\,\mathrm{Mpc}^{-1}$ for the case without the running of the spectral index, and $\Delta_{\mathcal{R}}^2(k_0) = 2.40 \pm 0.10 \times 10^{-9}$ and $n_s = 1.009 \pm 0.025$ and $\alpha_s = -0.019 \pm 0.025$ for that with the running of the spectral index [43].

Using the parametrization in Eq. (67), we can calculate the chemical potential for the μ-type distortions due to the Silk damping from Eqs. (42) and (66). Figure 5 shows the dependence of the chemical potential μ on n_s and α_s. Note that the effect of $\Delta_{\mathcal{R}}^2$ is just to scale the chemical potential.

Although the current constraint on CMB distortions by COBE/FIRAS can provide the limit on the primordial curvature perturbations, the obtained limit is looser than the constraint from the CMB anisotropies [46]. However, as shown in Fig. 5, since PIXIE and PRISM can detect μ-type distortions with $\mu \approx 5 \times 10^{-8}$ and $\mu \sim 10^{-9}$, respectively, the measurement of CMB distortions by PIXIE and PRISM may be comparable to or possibly stronger than the bounds on the primordial curvature perturbations by CMB observations such as WMAP. Therefore, these observations have the possibility to rule out some inflation models that produce the additional features on small scales. There are many

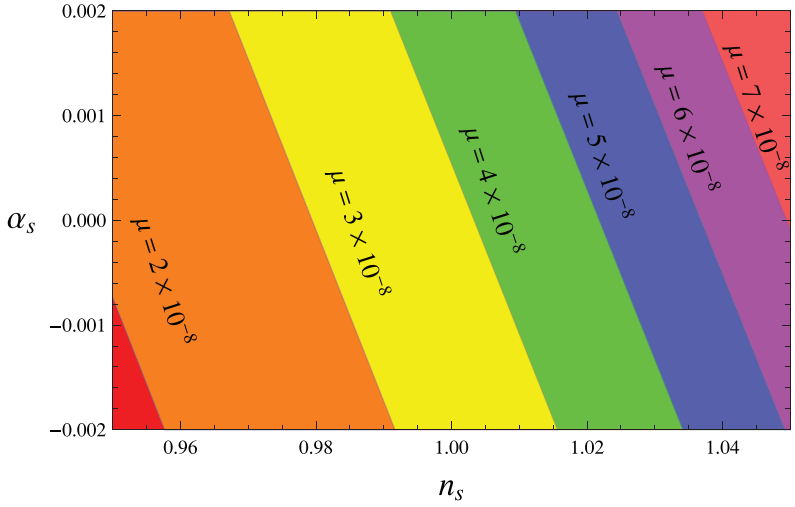

Fig. 5. The dependence of the chemical potential μ on n_s and α_s. Here we set $\Delta^2_{\mathcal{R}} = 2.4 \times 10^{-9}$. The figure is taken from Ref. [27].

papers forecasting possible constraints on generic models of $P_{\mathcal{R}}(k)$ at small scales, including the running of the spectral index, steps in the power spectrum, and bending of the spectrum, motivated by various inflation models [18,23,27,61,95].

The measurement of CMB distortions can provide a constraint not only on the power spectrum, but also on the non-Gaussianity of the primordial perturbations [7,34,86]. The primordial non-Gaussianity is an important observable in probing the physics in the early universe, especially the inflationary regime (for a recent review, see Ref. [5]). To represent non-Gaussianity, one can use the parameters $f_{\rm NL}$ and $\tau_{\rm NL}$, which respectively parametrize the bispectrum and the trispectrum of the primordial perturbations. Since the CMB distortion is proportional to the power spectrum of the primordial curvature perturbations, cross-correlations between the CMB distortion and the temperature anisotropy depend on the bispectrum of the primordial perturbations, and the auto-correlation of CMB distortion can measure the trispectrum [86]. However, Refs. [7,34] showed that the predicted constraint by PIXIE on the primordial non-Gaussianity is weaker than the current constraint provided by Planck, $f_{\rm NL}^{\rm local} = 2.7 \pm 5.8$ at 65% confidence level and $\tau_{\rm NL} < 2800$ at 95% confidence level [93]. Nevertheless, the measurement of CMB distortions is important for probing the primordial non-Gaussianity. Because CMB distortions are sensitive to small scales, they can still provide useful information for the scale dependence of primordial non-Gaussianity.

Isocurvature perturbations describe the fluctuations in the abundance ratio of the components, including dark matter, baryons, and neutrinos [9]. While single-field inflation models predict pure curvature perturbations as the primordial perturbations, some multi-field inflation models, including the curvaton [72] and axion models [71], can produce isocurvature perturbations. Therefore, the detection of isocurvature perturbations can discriminate between inflation models. Although large-scale observations rule out the pure isocurvature models, the existence of subdominant isocurvature perturbations cannot be excluded [43,82,92].

The effect of primordial isocurvature perturbations on the CMB distortions was first studied by Dent et al. [27]. Then, Chluba et al. performed a detailed investigation including the baryon, cold dark matter, neutrino density, and the velocity isocurvature modes [19]. The evolution of isocurvature perturbations is different from that of curvature perturbations (see e.g. Ref. [49]) and, thus, the

contribution of isocurvature perturbations to CMB distortions depends on the type of isocurvature modes. The contribution of both the CDM isocurvature and the baryon isocurvature perturbations are negligibly small unless the spectral index is very blue. On the other hand, the neutrino density isocurvature and the neutrino velocity isocurvature perturbations can contribute comparably to the curvature perturbations. Therefore, CMB distortions are sensitive to the presence of dark radiation or sterile neutrinos [19].

5.2. Negative distortions due to Bose–Einstein condensation

When baryons are non-relativistic, their adiabatic index is 5/3. This causes the baryon temperature to be proportional to $(1+z)^2$, and, thus, baryons cool faster than CMB photons. However, since electrons are tightly coupled with photons above $z > 500$, the photons keep heating up the baryons to the CMB temperature. In other words, the baryons cool the photons via the Compton scattering terms and the photons are transferred to lower frequencies. This is the opposite of the process caused by hot electrons. The photon distribution at high frequencies approaches a blackbody distribution with a lower electron temperature, while photons at low frequencies accumulate due to photon number conservation. That is, it is expected that Bose–Einstein condensation occurs.

However, Khatri et al. have shown that there is no actual condensation because this process is slow enough that the condensed photons are efficiently absorbed by double Compton scattering and bremsstrahlung [62]. Instead, the negative μ-type and y-type distortions arise. The total fractional energy loss of radiation due to the baryon cooling is given by the baryon-to-photon ratio. Therefore, the total fractional energy loss is tiny and corresponds to $Q/\rho_\gamma = -2.2 \times 10^{-9}$, where Q is the energy loss due to the baryon cooling in the μ-type distortion era. This partially cancels the energy injection due to the Silk damping of the primordial density fluctuations. Total cancellation can occur if, e.g., $n_s = 1.0$ and $dn_s/d\ln k = -0.038$. Therefore, there is a possibility that the μ-type distortion due to the Silk damping of the primordial perturbations with current-allowed cosmological parameters is strongly suppressed by this negative μ-type distortion.

5.3. Decay or annihilation of relic particles

Decay and annihilation of relic particles have the potential to produce observable CMB distortions [17,22,48,76,132]. Weakly interacting massive particles (WIMPs), which are attractive candidates for dark matter, are included in such particles. The degree of CMB distortions depends on the particle physics nature of these particles. Therefore, measurements of CMB distortions can provide a probe of particle physics and give a clue to the nature of dark matter.

5.3.1. Decaying particles. The decay of an unstable particle can release a large amount of energy into the CMB. There are many particle physics candidates including axions and sterile neutrinos [12,29]. The energy injection occurs when the decay rate becomes comparable with the Hubble rate. Therefore, the decay rate of particles that can generate CMB distortions corresponds to $\Gamma \sim 10^{-10} - 10^{-6}\,\mathrm{s}^{-1}$. On the other hand, e.g., the constraint on the particles with the decay rate $\Gamma < 10^{-1} - 10^{-2}\,\mathrm{s}^{-1}$ is obtained from Big Bang Nucleosynthesis (BBN) (e.g. Ref. [58]) and that with $\Gamma \lesssim 10^{-12}\,\mathrm{s}^{-1}$ is provided by the effect on the CMB anisotropies during the epochs of recombination and reionization (e.g. Ref. [134]). In particular, the stringent constraint for long-lifetime particles ($\Gamma < 10^{-2}\,\mathrm{s}^{-1}$) is obtained from the abundance of ^{3}He and D [57]. Depending on the models of decaying particles, their decay rate could be related to their mass. Therefore, the cosmological constraint on the decay rate is an important tool for the physics of dark matter.

The COBE/FIRAS upper limit on CMB distortions corresponds to $Q/\rho_\gamma < 10^{-6}$ [48]. Following the parametrization [16], the energy injection rate due to decaying particles is given by

$$\frac{d}{dz}\left(\frac{Q}{\rho_\gamma}\right) = f_X \frac{n_{\rm H}(z)\Gamma_X}{H(z)\rho_\gamma(z)(1+z)} e^{-\Gamma_X t}, \tag{68}$$

where Γ_X is the decay rate, $n_{\rm H}$ is the number density of hydrogen, and f_X is the model parameter that is related to the mass and the number density of the decaying particles. In this parametrization, the total injected energy is proportional to f_X/z_X, where z_X is the redshift of decay, $z_X \approx 4.8 \times 10^9 (\Gamma_X/1\,{\rm s}^{-1})^{1/2}$. Chluba has studied the feasibility of PIXIE to constrain the parameters f_X/z_X and z_X, calculating the spectral distortions in the large energy injection scenario, $Q/\rho_\gamma = 6.4 \times 10^{-6}$, and the small energy injection scenario, $Q/\rho_\gamma = 1.3 \times 10^{-7}$ [17]. In this work, it was shown that, within the sensitivity of PIXIE, 1% precision can be obtained for the parameter estimate of f_X/x_X and z_X.

5.3.2. Annihilating particles. Annihilation is one importation aspect of thermal relic particles like WIMPs. The "freeze-out" of the annihilation of these particles occurs long before the era of CMB distortions and the particle abundance is similar to the observed dark matter density [69]. In general, the freeze-out temperature is given by $T_f \sim m_X/25$, where m_X is the mass of the annihilating particle. However, even after freeze-out, annihilation of these particles happens continuously at a small rate. Therefore, the energy injection due to annihilation can produce CMB distortions.

The energy injection rate due to annihilating particles is given by

$$\frac{dQ}{dt} = f m_X \langle \sigma v_r \rangle n_X n_{\bar{X}}, \tag{69}$$

where f is the fraction of the annihilation energy density injected into the CMB energy density and n_X ($n_{\bar{X}}$) is the number density of the particle (anti-particle). In Eq. (69), $\langle \sigma v_r \rangle$ is the velocity-weighted annihilation cross section with the relative velocity between the annihilated particles v_r, where $\langle\ \rangle$ denotes the thermal average.

In the non-relativistic limit, the velocity-weighted annihilation cross section can be expanded as

$$\langle \sigma_{\rm ann} v_r \rangle = a + b v_r^2. \tag{70}$$

The coefficients a and b represent the s-wave and p-wave components, respectively.

Although the velocity-weighted cross section of the s-wave component is constant, that of the p-wave component depends on v_r^2. Because the relative velocity evolves as $(1+z)$, the p-wave contribution of the velocity-weighted cross section $\langle \sigma_{\rm ann} v_r \rangle$ is proportional to $(1+z)^2$. However, if the annihilation cross section is enhanced by the mechanism first described by Sommerfeld (Sommerfeld enhancement) [107], the redshift dependence is modified to $(1+z)$ [2,56]. This redshift dependence also arises for Majorana particles, which are relativistic even after freeze-out [44].

The first study of spectral distortions due to annihilation was performed by McDonald et al. [76]. Recently, Chluba updated the result for the constraint on the annihilation rate, introducing the parameter $f_{\rm ann}$, which parametrizes the energy injection rate as [17]

$$\frac{d}{dz}\left(\frac{Q}{\rho_\gamma}\right) = f_{\rm ann} \frac{n_{\rm H}(z)(1+z)^{n_\sigma}}{H(z)\rho_\gamma(z)}. \tag{71}$$

Hence $f_{\rm ann}$ is related to the abundance of the annihilating particle, its mass, and the cross section, and is normalized with the number density of hydrogen, $n_{\rm H}$. In Eq. (68), n_σ is determined by the

redshift dependence of the cross section. For the s-wave, $n_\sigma = 2$. In the p-wave case, $n_\sigma = 3$ for $\langle \sigma v_r \rangle \propto (1+z)$ and $n_\sigma = 4$ for $\langle \sigma v_r \rangle \propto (1+z)^2$.

In the case of s-wave annihilation, the tight constraint on the annihilation rate is obtained from the observation of the CMB anisotropies. WMAP provides the best current constraint, which corresponds to $f_{\rm ann} < 2 \times 10^{-23}\,{\rm eV\,s^{-1}}$. Although s-wave annihilation can produce both μ- and y-type distortions, the distortion generation is not efficient. In fact, the injected energy ratio with the WMAP constraint is $\Delta\rho_\gamma/\rho_\gamma \sim 8.3 \times 10^{-9}$ [33,50,106]. The resultant distortions are much smaller than the sensitivity of PIXIE, and the detection of these distortions at the 3σ level requires 10 times the sensitivity of PIXIE.

In the case of p-wave annihilation with $\langle \sigma v_r \rangle \propto (1+z)$, the energy injection occurs efficiently in higher redshifts, compared to that in the s-wave case. Therefore, the constraint from the CMB distortions is better than that from the CMB anisotropies. The constraint on μ-type distortion from COBE/FIRAS provides $f_{\rm ann} \lesssim 1.5 \times 10^{-24}\,{\rm eV\,s^{-1}}$ [17]. This constraint is also better than that obtained from BBN, corresponding to $f_{\rm ann} < 4 \times 10^{-24}\,{\rm eV\,s^{-1}}$. PIXIE can improve this constraint significantly. The 1σ detection limit of PIXIE can give $f_{\rm ann} \lesssim 2 \times 10^{-28}\,{\rm eV\,s^{-1}}$. For the case of $\langle \sigma v \rangle \propto (1+z)^2$, the cross section quickly becomes small as the redshift decreases. Therefore, if a large amount of energy injection occurs only in higher redshifts, one can expect a contribution to the μ-type distortions only. However, due to the redshift dependence, BBN provides a tighter constraint than a CMB distortion.

5.4. Primordial magnetic fields

Primordial magnetic fields might be relics of the early universe. Although such fields have not yet been detected, there are many studies predicting the existence of magnetic fields produced in the early universe, including the inflationary epoch, cosmological phase transitions, and the epoch of recombination (see Ref. [30] for a recent review).

Current upper limits on primordial magnetic fields are provided through CMB anisotropies (e.g., Refs. [103,130]) and large-scale structures [55,87,119]. These limits allow the existence of primordial magnetic fields with nano-Gauss comoving strength on Mpc scales. Recently, there have been some reports that observations of TeV blazars suggest the existence of magnetic fields in the intergalactic medium (IGM), the strength of which is larger than 10^{-17} gauss [83,120].

If primordial magnetic fields exist, they induce the photon–baryon fluid velocity through the Lorentz force before the recombination epoch. The fluid motions can be decomposed into three magnetohydrodynamic (MHD) modes, called the fast and slow magnetosonic and Alfvén modes. The fast and slow magnetosonic modes are compressive, and give the fluctuations of the plasma density and magnetic fields. On the other hand, Alfv́en modes are incompressive and give the fluctuations of magnetic fields.

Similar to the acoustic waves due to primordial perturbations, the energies of these modes dissipate through the viscosity of the photon–baryon fluid. However, these dissipation scales depend on the modes [53,109]. Although the damping scale of the fast modes is the same as that of the acoustic wave, the damping of the slow magnetosonic and Alfvén modes is complex. The slow magnetosonic and Alfv́en modes damp on scales $1/k$ larger than $1/(a\dot{\tau}_C v_A \cos\theta)$, where v_A is the Alfvén velocity in the radiation-dominant epoch, $v_A = B/\sqrt{16\pi\rho_\gamma/3}$, and θ is the angle between $\boldsymbol{B}$ and $\boldsymbol{k}$, while these MHD modes are over-damped and almost frozen on scales shorter than $1/(a\dot{\tau}_C v_A \cos\theta)$. As a result, these MHDmodes can survive below the Silk damping scale. When the wavelength $1/k$

becomes smaller than $1/(a\dot{\tau}_{\rm C})$, these MHD modes are damped again by occasional collisions of the fluid particles with background ones. As a result, the energy of magnetic fields below this damping scale is dissipated to plasma.

The effect of the MHD mode damping on the creation of CMB distortions was studied in Refs. [54,68]. The energy dissipation of magnetic fields is efficient between 400 pc and 0.6 Mpc. The COBE/FIRAS constraint on CMB distortions provides the constraint on magnetic fields, $B_0 < 40\,{\rm nG}$, where B_0 corresponds to the comoving magnetic field strength at 1 Mpc, when we assume that the power spectrum of magnetic fields is almost scale-invariant (the spectral index of magnetic fields $n_B = -2.9$). When the PIXIE sensitivity is applied, this constraint is improved to $B_0 < 0.8\,{\rm nG}$. Since the magnetic field dissipation is efficient on small scales, the limit of CMB distortions can give a stronger constraint for magnetic fields with a blue-tilted power spectrum. For example, the COBE/FIRAS constraint corresponds to $B_0 < 1.0\,{\rm nG}$ for $n_B = -2.6$.

Dissipated energy depends on the local magnetic field strength. In general, primordial magnetic fields are stochastic. Therefore, fluctuations of CMB distortions are expected from fluctuations in primordial magnetic field strength. The angular power spectrum of the CMB distortions was studied in Ref. [80]. Their result indicated that LiteBIRD and CMBpol can detect the angular power spectrum of y-type distortions due to magnetic fields with large tilts $n_B \gtrsim 0$ and strengths close to the current upper limit.

Even after the epoch of recombination, the magnetic fields can dissipate, and their energy is damped into the IGM by two processes [102]. One is ambipolar diffusion, which is caused by the relative velocity between neutral and residual ionized particles with the existence of magnetic fields. After the decoupling epoch, there exists a residual ionized particle corresponding to $x_e \sim 10^4$. The Lorentz force acts only on these residual ionized particles, and generates a velocity difference between the ionized and neutral particles. The collision of these particles damps this velocity difference and, as a result, leads to the dissipation of primordial magnetic fields. The second is the decay of the MHD turbulence. The nonlinear effect of the fluid velocity causes the decay of turbulent MHD modes, which transfers the magnetic energy to small scales where the energy is finally dissipated.

Reference [68] investigated the CMB distortion due to these dissipation mechanisms after the decoupling epoch. They show that the decay of the MHD turbulence makes dominant contributions and primordial magnetic fields of a few nano-Gauss can generate y-type distortion $y = 10^{-7}$, which can be detected by PIXIE at the 50σ level.

5.5. *Primordial black holes*

Primordial black holes (PBHs) could have formed in the early universe through the direct collapse of an overdensity region, whose scale corresponds to the horizon size at that time [13]. Therefore, although there is no direct evidence for their existence, the PBH mass function is expected to be a probe of primordial density fluctuations on small scales that cannot be accessed by the CMB and the large-scale-structure observations, and the constraints on the abundance of PBHs continue to be updated (for a recent review, see Ref. [14]).

It is known that PBHs eventually evaporate through thermal radiation with temperature $T_{\rm PBH} = \hbar c^3/8\pi G M k_{\rm B} \sim 10^{-7}(M/M_\odot)^{-1}$, known as Hawking radiation [38,39]. Accordingly, the evaporation time scale for a PBH with mass M is given by

$$\tau \sim \frac{G^2 M^3}{\hbar c^4} \sim 10^{64}\left(\frac{M}{M_\odot}\right)\,{\rm yr}. \tag{72}$$

Hence, PBHs with masses smaller than 10^{15} g have evaporated by the present epoch. Since such PBHs produce a large amount of photons in their evaporation, they play important roles as the sources of energy injections to the CMB.

Tashiro et al. studied CMB distortions induced by PBH evaporations [118]. It was shown that PBHs with $10^{11}\,\mathrm{g} < M < 10^{14}\,\mathrm{g}$ can contribute to produce CMB distortions. From the COBE/FIRAS constraint, they obtained the constraint on the PBH abundance:

$$\beta' < 10^{-21} \quad \text{for } 10^{11}\,\mathrm{g} \lesssim M \lesssim 10^{14}\,\mathrm{g}. \tag{73}$$

Here β' is defined as $\beta' \equiv \gamma^{1/2}(g_*/106.75)^{-1/4}\beta(M)$, where $\beta(M)$ denotes the mass fraction of PBHs at the time of formation, γ is a numerical factor that depends on the details of gravitational collapse, and g_* is the number of relativistic degrees of freedom. This constraint is weaker than the constraint from the BBN [14]. However, since the CMB distortions due to PBH evaporations are proportional to β', PIXIE and PRISM can improve the PBH constraint down to $\beta' \lesssim 10^{-24}$, slightly better than the BBN constraint.

The measurement of CMB distortions can also provide a constraint on the abundance of non-evaporating PBHs [98]. Massive PBHs could produce X-ray and UV photons through accretion of matter onto PBHs. Because these photons can ionize and heat the IGM, y-type distortion could be induced via Compton scattering of the CMB photons in heated IGM. Ricotti et al. showed that the upper limit of y-type distortion gives the best constraint on the existence of PBHs with masses smaller than 100 $M_\odot$ [98].

In addition to these, Ref. [88] studied the effect of the superradiant instabilities [121] of non-evaporating PBHs on CMB distortions.

5.6. Cosmic strings

A cosmic string is one of the topological defects that could be produced at phase transitions in the early universe [64] (see Refs. [42,123] for recent reviews). Hence, the detection of or a constraint on cosmic strings can allow us to access high-energy particle physics and the physics of the early universe.

In general, constraints on cosmic strings are provided in terms of the dimensionless parameter $G\mu_s$, where G is Newton's constant and μ_s is the mass per unit length of strings. The parameter $G\mu_s$ represents the strength of the gravitational interactions of strings. Currently, CMB anisotropy observations provide a constraint on $G\mu_s$. Recent Planck data give the limit $G\mu_s < 1.5 \times 10^{-7}$ [94].

In the context of CMB distortions, superconducting cosmic strings [129] are interesting. Moving through magnetized plasma, superconducting strings induce a large amount of electric current and emit electromagnetic radiation and particles [85,124]. Therefore, superconducting strings serve as sources to create CMB distortions [84,99,100,115]. Calculating CMB distortions due to superconducting strings, Tashiro et al. showed that the COBE/FIRAS upper limit on CMB distortions can provide a strong constraint on $G\mu_s$ of superconducting strings [115]. In particular, when the current is high enough that electromagnetic radiation determines the lifetime of their loops, the constraint by COBE/FIRAS suggests $G\mu_s \lesssim 10^{-12}$, which is much tighter than the CMB constraint. PIXIE can improve this limit down to $G\mu_s \lesssim 10^{-18}$.

Cosmic strings can induce density fluctuations. The current constraint allows 10% contributions of cosmic strings to large-scale-structure formations [94]. Before the epoch of recombination, these density fluctuations evolve as acoustic waves, and the energy of these acoustic waves is dissipated by Silk damping, similar to the primordial density fluctuations produced during the inflationary epoch.

However, because the induced density fluctuations have a red power spectrum, the dissipation energy is much smaller than the primordial density fluctuation case. Therefore, CMB distortions due to density fluctuations generated by cosmic strings are negligibly small [116].

5.7. Axion-like particles

The axion was introduced to solve the strong CP problem in quantum chromodynamics [89,126,127] and is now one of the best-motivated dark matter candidates. Besides, it is known that axion-like particles (ALPs) arise naturally in string theory [114,128], where a plenitude of light ALPs spanning many orders of magnitude in mass is provided [3].

ALPs generally couple to electromagnetic fields. Due to this coupling, a conversion between CMB photons and ALPs occurs in the IGM in the presence of primordial magnetic fields. This conversion can create CMB distortions [77,131]. In particular, large CMB distortions can be expected in the resonant conversion case. Plasma effects induce an effective mass for photons. Due to this effective mass, a resonant conversion between photons and axions with a mass the same as the effective photon mass arises.

Mirizzi et al. [78] first studied the CMB distortion due to the resonant conversion for the axion mass $m_A \gtrsim 10^{-14}$ eV. Later, the effect of the resonant conversion for $m_A < 10^{-14}$ eV was also evaluated in Ref. [117]. The limit on the CMB distortions provides a constraint on the product of the photon–ALP coupling constant g and the comoving strength of the primordial magnetic fields B. Future constraints from PIXIE or PRISM can provide a limit $gB < 10^{-16}\,\mathrm{GeV}^{-1} \cdot \mathrm{nG}$ for $m_A < 10^{-12}$ eV [117]. Although this result is not a direct constraint on g and B, it is significantly tighter than the product of the current upper limits on g [1] and B [55,87,103,130].

Since the distortion due to photon conversion is not a product of the thermalization process, its spectral shape is totally different from the μ-type and y-type distortions. Similar to the photon–axion conversion, the CMB distortions can be created in other photon-conversion models. The CMB distortions were investigated in the context of hidden photons [79], axionic dark radiation [41], and photon–graviton conversion [15].

6. Future prospects

Since the recent proposal of PIXIE and PRISM, the measurement of CMB distortions has received much attention as a new probe of the physics in the early universe. Just as WMAP provided a great deal of progress in cosmology by its precise measurement of the CMB anisotropy, the detailed measurement of the CMB frequency spectrum is expected to give exciting results on CMB spectral distortions. Therefore, precise predictions of the CMB distortions due to energy injections in the early universe are required. The recent development of numerical studies suggests the usability of the third type of CMB distortions, i-distortions. Because the energy release is generally continuous, the resultant frequency spectrum of the CMB consists of a combination of CMB distortions. However, the analytical prediction of the μ-type and y-type distortions is still useful for investigating the implications of the CMB distortion measurements for new physics.

The *anisotropy* of CMB distortions is an interesting new avenue that merits further study. Future observations such as LiteBIRD will have sufficient sensitivity and angular resolution to reveal the anisotropic features of CMB distortions. The anisotropic scale of CMB distortions is related to the scale of energy injection mechanisms.

Besides the Silk damping of acoustic waves and cooling baryons, there are other guaranteed distortions in standard cosmology that we have not discussed in this review (see Ref. [110] for a review).

The guaranteed distortions include the line emission features of hydrogen and helium at the epoch of recombination, resonant scattering by metals during the epoch of recombination, and y-type distortions from the epoch of reionization and clusters of galaxies. The sensitivity level of PIXIE and PRISM could detect these distortions. Detailed studies on these distortions will not only provide new information about the cosmological reionization and structure formations, but also help to search for the CMB distortions due to energy release in the early universe.

Clearly, the frequency spectrum of the CMB is a rich source of information on the early universe. We are optimistic that the observations of the CMB spectrum will give interesting results on CMB distortions in the near future.

Acknowledgement

It is a pleasure to thank Eray Sabancilar for helpful comments. This work was supported by the DOE.

References

[1] S. Andriamonje et al. (CAST Collaboration), J. Cosmol. Astropart. Phys., **2007**, 10 (2007).
[2] N. Arkani-Hamed, D. P. Finkbeiner, T. R. Slatyer, and N. Weiner, Phys. Rev. D **79**, 015014 (2009).
[3] A. Arvanitaki, S. Dimopoulos, S. Dubovsky, N. Kaloper, and J. March-Russell, Phys. Rev. D **81**, 123530 (2010).
[4] J. D. Barrow and P. Coles, Mon. Not. R. Astron. Soc., **248**, 52 (1991).
[5] N. Bartolo, E. Komatsu, S. Matarrese, and A. Riotto, Phys. Rep., **402**, 103 (2004).
[6] D. Baumann et al., AIP Conf. Proc., **1141**, 10 (2009).
[7] M. Biagetti, H. Perrier, A. Riotto, and V. Desjacques, Phys. Rev. D **87**, 063521 (2013).
[8] M. Birkinshaw, Phys. Rep., **310**, 97 (1999).
[9] M. Bucher, K. Moodley, and N. Turok, Phys. Rev. D **62**, 083508 (2000).
[10] C. Burigana, L. Danese, and G. de Zotti, Astrophys. J. **379**, 1 (1991).
[11] C. Burigana, L. Danese, and G. de Zotti, Astron. Astrophys., **246**, 49 (1991).
[12] D. Cadamuro, S. Hannestad, G. Raffelt, and J. Redondo, J. Cosmol. Astropart. Phys., **2011**, 3 (2011).
[13] B. J. Carr and S. W. Hawking, Mon. Not. R. Astron. Soc., **168**, 399 (1974).
[14] B. J. Carr, K. Kohri, Y. Sendouda, and J. Yokoyama, Phys. Rev. D **81**, 104019 (2010).
[15] P. Chen and T. Suyama, Phys. Rev. D **88**, 123521 (2013).
[16] X. Chen and M. Kamionkowski, Phys. Rev. D **70**, 043502 (2004).
[17] J. Chluba, Mon. Not. R. Astron. Soc., **436**, 2232 (2013).
[18] J. Chluba, A. L. Erickcek, and I. Ben-Dayan, Astrophys. J. **758**, 76 (2012).
[19] J. Chluba and D. Grin, Mon. Not. R. Astron. Soc., **434**, 1619 (2013).
[20] J. Chluba, R. Khatri, and R. A. Sunyaev, Mon. Not. R. Astron. Soc., **425**, 1129 (2012).
[21] J. Chluba, S. Y. Sazonov, and R. A. Sunyaev, Astron. Astrophys., **468**, 785 (2007).
[22] J. Chluba and R. A. Sunyaev, Mon. Not. R. Astron. Soc., **419**, 1294 (2012).
[23] S. Clesse, B. Garbrecht, and Y. Zhu, arXiv:1402.2257.
[24] R. A. Daly, Astrophys. J. **371**, 14 (1991).
[25] L. Danese and G. de Zotti, Riv. Nuovo Cimento, **7**, 277 (1977).
[26] L. Danese and G. de Zotti, Astron. Astrophys., **107**, 39 (1982).
[27] J. B. Dent, D. A. Easson, and H. Tashiro, Phys. Rev. D **86**, 023514 (2012).
[28] S. Dodelson, *Modern Cosmology* (Academic, Amsterdam, 2003).
[29] S. Dodelson and L. M. Widrow, Phys. Rev. Lett., **72**, 17 (1994).
[30] R. Durrer and A. Neronov, Astron. Astrophys. Rev., **21**, 62 (2013).
[31] D. J. Fixsen, E. S. Cheng, J. M. Gales, J. C. Mather, R. A. Shafer, and E. L. Wright, Astrophys. J. **473**, 576 (1996).
[32] D. J. Fixsen, A. Kogut, S. Levin, M. Limon, P. Lubin, P. Mirel, M. Seiffert, and E. Wollack, Astrophys. J. **612**, 86 (2004).
[33] S. Galli, F. Iocco, G. Bertone, and A. Melchiorri, Phys. Rev. D **80**, 023505 (2009).
[34] J. Ganc and E. Komatsu, Phys. Rev. D **86**, 023518 (2012).
[35] M. Gervasi, M. Zannoni, A. Tartari, G. Boella, and G. Sironi, Astrophys. J. **688**, 24 (2008).

[36] H. P. Gush, M. Halpern, and E. H. Wishnow, Phys. Rev. Lett., **65**, 537 (1990).
[37] A. H. Guth and S.-Y. Pi, Phys. Rev. Lett., **49**, 1110 (1982).
[38] S. W. Hawking, Nature, **248**, 30 (1974).
[39] S. W. Hawking, Commun. Math. Phys., **43**, 199 (1975).
[40] S. W. Hawking, Phys. Lett. B **115**, 295 (1982).
[41] T. Higaki, K. Nakayama, and F. Takahashi, J. Cosmol. Astropart. Phys., **2013**, 30 (2013).
[42] M. B. Hindmarsh and T. W. B. Kibble, Rep. Prog. Phys., **58**, 477 (1995).
[43] G. Hinshaw et al., Astrophys. J. Suppl., **208**, 19 (2013).
[44] C. M. Ho and R. J. Scherrer, Phys. Rev. D **87**, 065016 (2013).
[45] M. Hazumi et al., Space Telescopes and Instrumentation 2012: Optical, Infrared, and Millimeter Wave. Proc. of the SPIE, Vol. 8442, 9 pp. (2012).
[46] W. Hu, D. Scott, and J. Silk, Astrophys. J. Lett., **430**, L5 (1994).
[47] W. Hu and J. Silk, Phys. Rev. D **48**, 485 (1993).
[48] W. Hu and J. Silk, Phys. Rev. Lett., **70**, 2661 (1993).
[49] W. Hu and N. Sugiyama, Astrophys. J. **471**, 542 (1996).
[50] G. Hütsi, J. Chluba, A. Hektor, and M. Raidal, Astron. Astrophys., **535**, A26 (2011).
[51] A. F. Illarionov and R. A. Siuniaev, Sov. Astron., **18**, 413 (1975).
[52] A. F. Illarionov and R. A. Siuniaev, Sov. Astron., **18**, 691 (1975).
[53] K. Jedamzik, V. Katalinić, and A. V. Olinto, Phys. Rev. D **57**, 3264 (1998).
[54] K. Jedamzik, V. Katalinić, and A. V. Olinto, Phys. Rev. Lett., **85**, 700 (2000).
[55] T. Kahniashvili, Y. Maravin, A. Natarajan, N. Battaglia, and A. G. Tevzadze, Astrophys. J. **770**, 47 (2013).
[56] M. Kamionkowski and S. Profumo, Phys. Rev. Lett., **101**, 261301 (2008).
[57] M. Kawasaki, K. Kohri, and T. Moroi, Phys. Rev. D **71**, 083502 (2005).
[58] M. Kawasaki, K. Nakayama, and M. Senami, J. Cosmol. Astropart. Phys., **2008**, 9 (2008).
[59] R. Khatri and R. A. Sunyaev, J. Cosmol. Astropart. Phys., **2012**, 16 (2012).
[60] R. Khatri and R. A. Sunyaev, J. Cosmol. Astropart. Phys., **2012**, 38 (2012).
[61] R. Khatri and R. A. Sunyaev, J. Cosmol. Astropart. Phys., **2013**, 26 (2013).
[62] R. Khatri, R. A. Sunyaev, and J. Chluba, Astron. Astrophys., **540**, A124 (2012).
[63] R. Khatri, R. A. Sunyaev, and J. Chluba, Astron. Astrophys., **543**, A136 (2012).
[64] T. W. B. Kibble, J. Phys. A: Math. Gen., **9**, 1387 (1976).
[65] A. Kogut et al., J. Cosmol. Astropart. Phys., **2011**, 25 (2011).
[66] A. S. Kompaneets, JETP Lett., **4**, 730 (1957).
[67] A. Kosowsky and M. S. Turner, Phys. Rev. D **52**, 1739 (1995).
[68] K. E. Kunze and E. Komatsu, J. Cosmol. Astropart. Phys., **2014**, 9 (2014).
[69] B. W. Lee and S. Weinberg, Phys. Rev. Lett., **39**, 165 (1977).
[70] A. P. Lightman, Astrophys. J. **244**, 392 (1981).
[71] D. H. Lyth, Phys. Lett. B **236**, 408 (1990).
[72] D. H. Lyth and D. Wands, Phys. Lett. B **524**, 5 (2002).
[73] C.-P. Ma and E. Bertschinger, Astrophys. J. **455**, 7 (1995).
[74] J. C. Mather et al., Astrophys. J. **420**, 439 (1994).
[75] J. C. Mather et al., Astrophys. J. Lett., **354**, L37 (1990).
[76] P. McDonald, R. J. Scherrer, and T. P. Walker, Phys. Rev. D **63**, 023001 (2001).
[77] A. Mirizzi, G. G. Raffelt, and P. D. Serpico, Phys. Rev. D **72**, 023501 (2005).
[78] A. Mirizzi, J. Redondo, and G. Sigl, J. Cosmol. Astropart. Phys., **2009**, 1 (2009).
[79] A. Mirizzi, J. Redondo, and G. Sigl, J. Cosmol. Astropart. Phys., **2009**, 26 (2009).
[80] K. Miyamoto, T. Sekiguchi, H. Tashiro, and S. Yokoyama, Phys. Rev. D **89**, 063508 (2014).
[81] V. F. Mukhanov and G. V. Chibisov, Sov. J. Exp. Theor. Phys. Lett., **33**, 532 (1981).
[82] S. Muya Kasanda, C. Zunckel, K. Moodley, B. A. Bassett, and P. Okouma, J. Cosmol. Astropart. Phys., **2012**, 21 (2012).
[83] A. Neronov and I. Vovk, Science, **328**, 73 (2010).
[84] J. P. Ostriker and C. Thompson, Astrophys. J. Lett., **323**, L97 (1987).
[85] J. P. Ostriker, C. Thompson, and E. Witten, Phys. Lett. B **180**, 231 (1986).
[86] E. Pajer and M. Zaldarriaga, Phys. Rev. Lett., **109**, 021302 (2012).
[87] K. L. Pandey and S. K. Sethi, Astrophys. J. **762**, 15 (2013).
[88] P. Pani and A. Loeb, Phys. Rev. D **88**, 041301 (2013).

[89] R. D. Peccei and H. R. Quinn, Phys. Rev. Lett., **38**, 1440 (1977).
[90] P. J. E. Peebles and J. T. Yu, Astrophys. J. **162**, 815 (1970).
[91] A. A. Penzias and R. W. Wilson, Astrophys. J. **142**, 419 (1965).
[92] Planck Collaboration, arXiv:1303.5082.
[93] Planck Collaboration, arXiv:1303.5084.
[94] Planck Collaboration, arXiv:1303.5085.
[95] B. A. Powell, arXiv:1209.2024.
[96] PRISM Collaboration, arXiv:1306.2259.
[97] C. L. Reichardt et al., Astrophys. J. **755**, 70 (2012).
[98] M. Ricotti, J. P. Ostriker, and K. J. Mack, Astrophys. J. **680**, 829 (2008).
[99] N. Sanchez and M. Signore, Phys. Lett. B **219**, 413 (1989).
[100] N. Sanchez and M. Signore, Phys. Lett. B **241**, 332 (1990).
[101] M. Seiffert, D. J. Fixsen, A. Kogut, S. M. Levin, M. Limon, P. M. Lubin, P. Mirel, J. Singal, T. Villela, E. Wollack, and C. A. Wuensche, Astrophys. J. **734**, 6 (2011).
[102] S. K. Sethi and K. Subramanian, Mon. Not. R. Astron. Soc., **356**, 778 (2005).
[103] J. R. Shaw and A. Lewis, Phys. Rev. D **86**, 043510 (2012).
[104] J. Silk, Astrophys. J. **151**, 459 (1968).
[105] J. Singal, D. J. Fixsen, A. Kogut, S. Levin, M. Limon, P. Lubin, P. Mirel, M. Seiffert, and E. J. Wollack, Astrophys. J. **653**, 835 (2006).
[106] T. R. Slatyer, N. Padmanabhan, and D. P. Finkbeiner, Phys. Rev. D **80**, 043526 (2009).
[107] A. Sommerfeld, Ann. Phys., **403**, 257 (1931).
[108] A. A. Starobinsky, Phys. Lett. B **117**, 175 (1982).
[109] K. Subramanian and J. D. Barrow, Phys. Rev. D **58**, 083502 (1998).
[110] R. A. Sunyaev and R. Khatri, Int. J. Mod. Phys. D **22**, 30014 (2013).
[111] R. A. Sunyaev and Y. B. Zeldovich, Astrophys. Space Sci., **9**, 368 (1970).
[112] R. A. Sunyaev and Y. B. Zeldovich, Astrophys. Space Sci., **7**, 3 (1970).
[113] R. A. Sunyaev and Y. B. Zeldovich, Astrophys. Space Sci., **7**, 20 (1970).
[114] P. Svrcek and E. Witten, J. High Energy Phys., **2006**, 51 (2006).
[115] H. Tashiro, E. Sabancilar, and T. Vachaspati, Phys. Rev. D **85**, 103522 (2012).
[116] H. Tashiro, E. Sabancilar, and T. Vachaspati, J. Cosmol. Astropart. Phys., **2013**, 35 (2013).
[117] H. Tashiro, J. Silk, and D. J. E. Marsh, Phys. Rev. D **88**, 125024 (2013).
[118] H. Tashiro and N. Sugiyama, Phys. Rev. D **78**, 023004 (2008).
[119] H. Tashiro, K. Takahashi, and K. Ichiki, Mon. Not. R. Astron. Soc., **424**, 927 (2012).
[120] F. Tavecchio, G. Ghisellini, L. Foschini, G. Bonnoli, G. Ghirlanda, and P. Coppi, Mon. Not. R. Astron. Soc., **406**, L70 (2010).
[121] S. A. Teukolsky and W. H. Press, Astrophys. J. **193**, 443 (1974).
[122] Planck Collaboration, arXiv:0604069 [astro-ph].
[123] A. Vilenkin and E. P. S. Shellard, *Cosmic Strings and Other Topological Defects* (Cambridge University Press, Cambridge, UK, 2000).
[124] A. Vilenkin and T. Vachaspati, Phys. Rev. Lett., **58**, 1041 (1987).
[125] S. Weinberg, Astrophys. J. **168**, 175 (1971).
[126] S. Weinberg, Phys. Rev. Lett., **40**, 223 (1978).
[127] F. Wilczek, Phys. Rev. Lett., **40**, 279 (1978).
[128] E. Witten, Phys. Lett. B **149**, 351 (1984).
[129] E. Witten, Nucl. Phys. B **249**, 557 (1985).
[130] D. G. Yamazaki, T. Kajino, G. J. Mathews, and K. Ichiki, Phys. Rep., **517**, 141 (2012).
[131] T. Yanagida and M. Yoshimura, Phys. Lett. B **202**, 301 (1988).
[132] Y. B. Zel'dovich, A. F. Illarionov, and R. A. Syunyaev, Sov. J. Exp. Theor. Phys., **35**, 643 (1972).
[133] Y. B. Zeldovich and R. A. Sunyaev, Astrophys. Space Sci., **4**, 301 (1969).
[134] L. Zhang, X. Chen, M. Kamionkowski, Z.-G. Si, and Z. Zheng, Phys. Rev. D **76**, 061301 (2007).